Monthly Notices
of the
ROYAL ASTRONOMICAL SOCIETY

MNRAS **491,** 3891–3899 (2020)
Advance Access publication 2019 November 23

doi:10.1093/mnras/stz3278

Properties of reionization-era galaxies from *JWST* luminosity functions and 21-cm interferometry

Jaehong Park [1]★ Nicolas Gillet [1] Andrei Mesinger[1] and Bradley Greig [2,3]

[1] *Scuola Normale Superiore, Piazza dei Cavalieri 7, I-56126 Pisa, Italy*
[2] *ARC Centre of Excellence for All-Sky Astrophysics in 3 Dimensions (ASTRO 3D), University of Melbourne, VIC 3010, Australia*
[3] *School of Physics, The University of Melbourne, Parkville, VIC 3010, Australia*

Accepted 2019 November 18. Received 2019 November 13; in original form 2019 August 22

ABSTRACT

Upcoming observations will probe the first billion years of our Universe in unprecedented detail. Foremost among these are 21-cm interferometry with the Hydrogen Epoch of Reionization Arrays (HERA) and the Square Kilometre Array (SKA), and high-z galaxy observations with the *James Webb Space Telescope* (*JWST*). Here, we quantify how observations from these instruments can be used to constrain the astrophysics of high-z galaxies. We generate several mock *JWST* luminosity functions (LFs) and SKA1 21-cm power spectra, which are consistent with current observations, but assume different properties for the unseen, ultrafaint galaxies driving the epoch of reionization (EoR). Using only *JWST* data, we predict up to a factor of 2–3 improvement (compared with *Hubble Space Telescope, HST*) in the fractional uncertainty of the star formation rate to halo mass relation and the turnover magnitude. Most parameters regulating the ultraviolet (UV) galaxy properties can be constrained at the level of $\sim$10 per cent or better, *if* either (i) we are able to better characterize systematic lensing uncertainties than currently possible; or (ii) the intrinsic LFs peak at magnitudes brighter than $M_{\rm UV} \lesssim -13$. Otherwise, improvement over *HST*-based inference is modest. When combining with upcoming 21-cm observations, we are able to significantly mitigate degeneracies, and constrain all of our astrophysical parameters, even for our most pessimistic assumptions about upcoming *JWST* LFs. The 21-cm observations also result in an order of magnitude improvement in constraints on the EoR history.

Key words: galaxies: high-redshift – intergalactic medium – dark ages, reionization, first stars – diffuse radiation – early Universe – cosmology: theory.

1 INTRODUCTION

Recent years have witnessed remarkable progress in understanding the timing of the epoch of reionization (EoR). Aided primarily by high-redshift quasar (QSO) spectra (e.g. Mortlock et al. 2011; McGreer, Mesinger & D'Odorico 2015; Bañados et al. 2018) and the optical depth to the cosmic microwave background (CMB, e.g. Planck Collaboration et al. 2016b, 2018), we can estimate that the mid-point of the EoR (when the volume-averaged neutral fraction was $\bar{x}_{\rm HI} = 0.5$) was around $z \sim 7.5 \pm 1$ (e.g. Mitra, Roy Choudhury & Ferrara 2015; Planck Collaboration et al. 2016b; Greig & Mesinger 2017a; Price et al. 2018; Gorce et al. 2018) with a maximum of a few per cent of the intergalactic medium (IGM) remaining neutral by $z = 6$ (McGreer et al. 2015; although the final overlap stages can extend to $z \sim$ 5–6, Lidz et al. 2007; Mesinger 2010; Keating et al. 2019).

The next few years will see us moving away from putting points on the $\bar{x}_{\rm HI}$ versus z plane, towards a deeper understanding of the galaxies that are responsible for the EoR. This will primarily be enabled by two ground-breaking observations: (i) near-infrared high-z galaxy studies with the *James Webb Space Telescope* (*JWST*; Gardner et al. 2006) and (ii) measurements of the 3D structure of the EoR with next-generation 21-cm interferometers like Hydrogen Epoch of Reionization Array (HERA,[1] DeBoer et al. 2017) and Square Kilometre Array (SKA;[2] Mellema et al. 2013; Koopmans et al. 2015).

Although *JWST* will enable resolved spectroscopy of high-z galaxies, such detailed studies will be limited to relatively bright and rare objects (e.g. Stark 2016; Shapley et al. 2017; Williams et al. 2018; Chevallard et al. 2019). The bulk of the high-z galaxy population will be studied primarily by counting the number

★ E-mail: jaehong.park@sns.it

[1] http://reionization.org
[2] https://astronomers.skatelescope.org

per volume which fall in a given non-ionizing ultraviolet (UV) magnitude bin, the so-called rest-frame UV luminosity functions (UV LFs). *JWST* should extend our knowledge of high-z LFs by pushing 1–2 mag deeper than current observations with Hubble (e.g. Salvaterra, Ferrara & Dayal 2011; Dayal et al. 2013; Shimizu et al. 2014; O'Shea et al. 2015; Finkelstein 2016; Wilkins et al. 2017; Cowley et al. 2018; Tacchella et al. 2018; Williams et al. 2018; Yung et al. 2019). This will allow us to push blank field LFs to magnitudes fainter than $M_{\rm UV} \gtrsim -17$; such faint magnitudes are currently accessible only through cluster lensing, and are thus susceptible to large systematic uncertainties including lens modelling and completeness corrections (e.g. Bouwens et al. 2016; Livermore, Finkelstein & Lotz 2017; Atek et al. 2018; Ishigaki et al. 2018).

On the other hand, the 21-cm line from neutral hydrogen will enable us to map the IGM on large scales, during the first billion years. From these large-scale 21-cm structures, we can *indirectly* infer average properties of high-redshift galaxies, albeit with some degeneracies (e.g. McQuinn et al. 2007; Pober et al. 2015; Greig & Mesinger 2015, 2017b; Ross et al. 2019). These properties include the stellar mass fraction, the gas fraction, the star formation rate (SFR), the escape fraction, X-ray luminosities, etc.

In Park et al. (2019), we showed that high-z LFs and 21-cm interferometry are complementary observations, helping us nail down the properties of high-z galaxies, and ameliorating the degeneracies present when each is considered separately. We used current LF observations obtained with the *Hubble* telescope, combining them with a mock 21-cm observation from a 1000 h integration with the HERA instrument. In this work, we quantify the additional constraints on high-z galaxy properties available with deeper LF observations, such as might be expected from *JWST*.

This paper is organized as follows. In Section 2, we describe our mock LF and 21-cm observations. Then, we show the corresponding constraints on astrophysical parameters in Section 3. In Section 4, we summarize our results. We assume a standard Λ cold dark matter cosmology based on *Planck* 2016 (Planck Collaboration et al. 2016a): (h, $\Omega_{\rm m}$, $\Omega_{\rm b}$, Ω_Λ, σ_8, $n_{\rm s}$) = (0.678, 0.308, 0.0484, 0.692, 0.815, 0.968). Unless stated otherwise, we quote all quantities in comoving units, and when we refer to the UV magnitude, this corresponds to the rest-frame 1500Å AB magnitude.

2 DATA SETS

As in Park et al. (2019), we compute the likelihood of our model parameters using two main data sets: the rest-frame UV LFs at high-z and mock 21-cm power spectra (PS) measurements. The main difference in this work is that instead of using current LFs observations from *Hubble*, we use deeper mock LFs, roughly corresponding to what we should get with *JWST*.

In addition to these two mock data sets, we also include in our likelihood calculation the two most robust constraints on EoR timing currently available: (i) the electron scattering optical depth to the CMB, $\tau_{\rm e} = 0.058 \pm 0.012 (1\sigma)$ from (Planck Collaboration et al. 2016b); and (ii) the upper limit of the neutral fraction, $\bar{x}_{\rm HI} < 0.06 + 0.05(1\sigma)$ at $z = 5.9$ from the fraction of dark pixels in QSO spectra (McGreer et al. 2015). These EoR timing measurements allow a rough estimate of the ionizing escape fraction, when combined also with the observed LFs (e.g. Kuhlen & Faucher-Giguère 2012; Mitra, Ferrara & Choudhury 2013; Mitra, Roy Choudhury & Ferrara 2015; Robertson et al. 2013, 2015; Price, Trac & Cen 2016), but become superfluous when 21-cm observations become available (Park et al. 2019).

2.1 Mock *JWST* LFs

Our mock LFs are taken from the GAlaxy Formation For the Eo (GAFFER) simulation suite (Gillet et al. in preparation). GAFFER is comprised of ∼800 fully coupled hydroradiative transfer cosmological simulations aiming to characterize the growth of dwarf galaxies during the EoR. Using the numerical code EMMA (Aubert, Deparis & Ocvirk 2015), we vary five astrophysical/numerical parameters governing galaxy formation: the star formation efficiency (ϵ_*), the interstellar medium overdensity threshold for star formation (δ_*), the supernova feedback efficiency ($\epsilon_{\rm SN}$), the subgrid ionizing escape fraction ($f_{\rm esc}$), and the mass of the numerical star particle (M_* [$M_\odot$]). For more details on how these parameters affect the star formation and feedback models in EMMA, we refer the reader to Deparis, Aubert & Ocvirk (2016), Deparis et al. (2019), and Deparis et al. (in preparation). Most of the simulation boxes are 10 Mpc on a side, with haloes above $\sim 2 \times 10^8 M_\odot$ being resolved with >100 dark matter particles.

For each simulation, we compute the corresponding LFs by assuming a constant conversion factor between a galaxy's SFR (averaged over the previous 10 Myr)[3] and its 1500 Å UV luminosity: $\dot{M}_* = \mathcal{K}_{\rm UV} \times L_{\rm UV}$, with $\mathcal{K}_{\rm UV} = 1.15 \times 10^{-28} {\rm M}_\odot\,{\rm yr}^{-1}/{\rm erg\,s}^{-1}\,{\rm Hz}^{-1}$ consistent with a Salpeter initial mass function with a ∼10 per cent solar metallicity (cf. Kennicutt 1998; Madau & Dickinson 2014). We do not model dust; thus our mock LFs would correspond to dust-corrected ones. However, since we concern ourselves with faint galaxies which dominate the photon budget during reionization, dust is unlikely to require a large correction over our magnitude range (e.g. Finkelstein et al. 2012; Dunlop et al. 2013; Bouwens et al. 2015b; Cullen et al. 2017; Wilkins et al. 2017; Yung et al. 2019; Ma et al. 2019; Vogelsberger et al. 2019).

From the GAFFER simulation suite, we select two simulations to use as mock *JWST* LFs. These two simulations have LFs which are both within 1σ of current observational constraints (e.g. Gillet et al. 2019; see Fig. 1) but were chosen to have different behaviour at the faint end. Detecting a turnover at brighter magnitudes with *JWST* would be easier than detecting it at fainter magnitudes; thus we take these two models to bracket the expected range. Below we denote mock observations based on the simulation with a turnover at brighter magnitudes with the suffix '-B', and those based on the simulation with a turnover at fainter magnitudes with the suffix '-F'. The difference of parameters of the two mock simulations is shown in Table 1. The *Mock*-F has fainter turnover magnitudes, meaning that it has a higher SFR than *Mock*-B, even if *Mock*-F has a lower star formation efficiency (ϵ_*). The difference is due to a stronger SNe and photoheating feedback from reionization in *Mock*-B (ϵ_* and $f_{\rm esc}$) (in fact the difference is due to the interplay of the five parameters and will be analysed in detail in Gillet et al., in preparation).

Mock observations are constructed from the galaxy number densities, $\phi(M_{\rm UV})$, in these two simulations. For consistency, we use the same galaxy number counts to make both *JWST* and *Hubble Space Telescope* (*HST*) mock LFs. For the mock *HST* LFs, we use the same magnitude bins with the observational data from Bouwens et al. (2016) for redshift 6, Bouwens et al. (2015a) for redshifts 7 and 8, and Oesch et al. (2017) for redshift 10, resulting in the

[3]We note that had we chosen a longer time-frame over which to average the SFR, the drop at faint magnitudes ($M_{\rm UV}$>−10) seen in Fig. 1 would be less steep; however, this does not have a notable effect on the observable luminosity range.

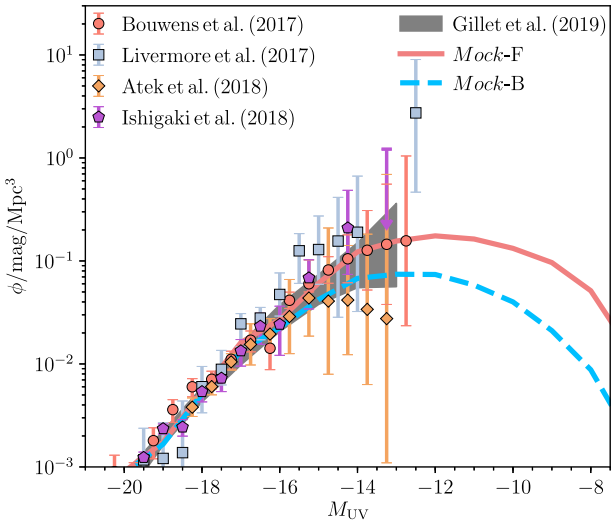

Figure 1. Simulated LFs at $z = 6$. These simulations were used to build the two sets of mock *JWST* LFs shown in Fig. 2. These were chosen because they agree with current constraints (the 68 per cent CL from Gillet, Mesinger & Park 2019 are denoted with the shaded area) but are very different at the ultrafaint end. For comparison, we show the rest-frame UV LFs observed from various groups that are used to obtain the 68 per cent CL We note that the Livermore et al. (2017) are unpublished versions (Livermore private communication), which correct the published ones for Eddington bias, bringing down some of the faintest points by up to a factor of two.

Table 1. Parameters used in the GAFFER simulation suite to generate mock LFs.

Parameters	*Mock*-F	*Mock*-B
ϵ_*	0.0046	0.0062
δ_*	26.422	56.631
$f_{\rm esc}$	0.1405	0.8121
M_* [$M_\odot$]	40347	7489
$\epsilon_{\rm SN}$	0.0051	0.0283

same magnitude cut-off at the faint end with these observations. We also use the same uncertainties from the foregoing observations, allowing for a direct comparison with the resulting constraints from Park et al. (2019). In each bin, the error is evaluated as the maximum of the observational uncertainty ($\sigma_{\rm OBS}$) and the Poisson error in the bin due to the finite simulation volume of the simulations ($\sigma_{\rm P}$). Over most of the range of interest, specifically $M_{\rm UV} > -18$, the observational uncertainties dominate over the cosmic variance. Moreover, we enforce that the uncertainty has to be greater than 20 per cent of the galaxy density ($\sigma \geq 0.2\phi$), taking this to be a systematic 'floor' (Bouwens, private communication). By construction, the *HST* mocks are entirely consistent with current *HST* observations.

JWST will detect fainter galaxies than is available in the current *HST* observations. Although the predicted detection limits depend on their assumption (e.g. detection depth for point source and exposure time), the agreement is that *JWST* will obtain faint galaxies ∼2 mag deeper than the current *HST* (e.g. Salvaterra et al. 2011; Dayal et al. 2013; Shimizu et al. 2014; O'Shea et al. 2015; Finkelstein 2016; Wilkins et al. 2017; Cowley et al. 2018; Tacchella et al. 2018; Williams et al. 2018; Yung et al. 2019). From the fact, we build the mock *JWST* LFs by extending the mock *HST* LFs 1.5 magnitudes deeper. Although, in principle, error bars should be computed considering specific volumes of specific observational programs, simply extending the *HST* LFs by 1.5 mag is a reasonable approximation for what is achievable with *JWST* (Finkelstein 2016; Bouwens & Oesch, private communication). Specifically, we take:

$$\sigma_{\rm JWST}(M_{\rm UV}) = \begin{cases} \sigma_{\rm HST}(M_{\rm UV} - 1.5) & \text{if } M_{\rm UV} > -14.5 \\ \sigma_{\rm HST}(M_{\rm UV}) & \text{if } M_{\rm UV} < -18 \\ 0.2\phi(M_{\rm UV}) & \text{if } -18 < M_{\rm UV} < -14.5 \end{cases} \quad (1)$$

with the Poisson-dominated bright-end taken to have the same errors as are currently available for *HST*, and the intermediate regime having 20 per cent systematic errors, similar to what is available currently from *HST* programs. As for *HST*, we only include lensed galaxies in the $z \sim 6$ *JWST* LFs. Although lensing might push the higher redshift LFs a bit deeper, the redshift selection efficiency of cluster lensing falls rapidly beyond $z > 6$–7 (e.g. Atek et al. 2015). Even if such galaxies are found in sufficient numbers to construct LFs, the associated large systematic uncertainties make them unlikely to affect our main results.

The resulting mock LFs are shown in Fig. 2, for both *HST* and *JWST* error bars, as well as for both of our simulations. As mentioned previously, LFs which have an intrinsic turnover at fainter (brighter) magnitudes are denoted with the qualifiers '-F' ('-B').

2.2 Mock 21-cm signal

We create a mock cosmic 21-cm signal using the public code 21CMFAST.[4] 21CMFAST (Mesinger & Furlanetto 2007; Mesinger, Furlanetto & Cen 2011) generates the evolved density and corresponding peculiar velocity fields by applying second-order Lagrangian perturbation theory (e.g. Scoccimarro 1998) on a high-resolution realization of a Gaussian random field. Then, 21CMFAST estimates the ionization field from the density field using an excursion-set approach (e.g. Furlanetto, Zaldarriaga & Hernquist 2004), while the spin temperature evolution is computed by integrating the cosmic X-ray and soft UV backgrounds back along the light-cone for each simulation cell. We use the latest version introduced in Park et al. (2019), allowing us to tie the galactic radiation sources to the corresponding UV LFs (cf. http://homepage.sns.it/mesinger/Videos/parameter_variation.mp4). Here, we briefly summarize the free parameters in the model; for more details on the simulation and the astrophysical parameters, readers are referred to Park et al. (2019).

We assume the average properties of high-z galaxies depend on their host dark matter halo mass (e.g. Behroozi & Silk 2015; Sun & Furlanetto 2016; Dayal & Ferrara 2018; Salcido, Bower & Theuns 2019). Specifically, we parametrize the typical stellar mass of galaxies with a power-law dependence on the total halo mass, $M_{\rm h}$:

$$M_*(M_{\rm h}) = f_{*,10}\left(\frac{M_{\rm h}}{10^{10}{\rm M}_\odot}\right)^{\alpha_*}\left(\frac{\Omega_{\rm b}}{\Omega_{\rm m}}\right)M_{\rm h} \quad (2)$$

where $f_{*,10}$ is the normalization (i.e. the fraction of galactic baryons in stars for haloes with a mass of $10^{10}{\rm M}_\odot$) and α_* is the power-law index. Then, the SFR is defined as

$$\dot{M}_*(M_{\rm h}, z) = \frac{M_*}{t_* H(z)^{-1}}, \quad (3)$$

[4]https://github.com/andreimesinger/21cmFAST

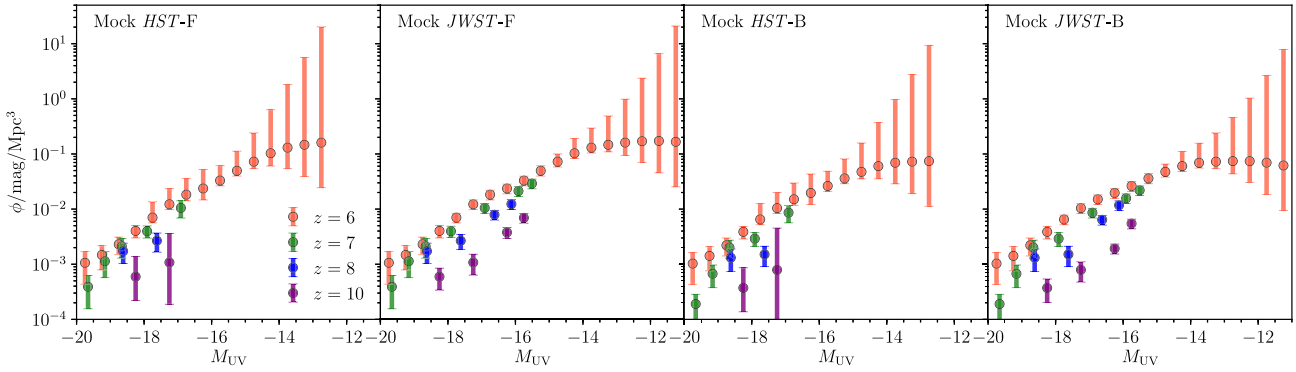

Figure 2. *HST* and *JWST* LF mock observations used for parameter recovery. LFs corresponding to the simulation with a turnover at brighter (fainter) magnitudes are denoted with '-B' ('-F').

where $H(z)^{-1}$ is the Hubble time and t_* is a free parameter regulating the star formation time-scale.

Similarly, we define the ionizing UV escape fraction as

$$f_{\rm esc}(M_{\rm h}) = f_{\rm esc,10}\left(\frac{M_{\rm h}}{10^{10}{\rm M}_\odot}\right)^{\alpha_{\rm esc}}, \quad (4)$$

where $f_{\rm esc,\,10}$ is the normalization of the escape fraction and $\alpha_{\rm esc}$ is a power-law index.

Since small haloes are unable to host star-forming galaxies due to their limited gas reservoir from inefficient cooling and/or feedback (e.g. Shapiro, Giroux & Babul 1994; Giroux, Sutherland & Shull 1994; Hui & Gnedin 1997; Barkana & Loeb 2001; Springel & Hernquist 2003; Okamoto, Gao & Theuns 2008; Mesinger & Dijkstra 2008; Sobacchi & Mesinger 2013), we introduce a duty cycle quantifying the fraction of haloes which host galaxies via

$$f_{\rm duty}(M_{\rm h}) = \exp\left(-\frac{M_{\rm turn}}{M_{\rm h}}\right), \quad (5)$$

Here $M_{\rm turn}$ is a characteristic mass below which the fraction of haloes hosting stars/galaxies exponentially decreases. For reference, $M_{\rm turn} \sim 10^8 M_\odot$ at $z \sim 10$ for a virial temperature of 10^4 K (corresponding to the atomic cooling threshold).

The corresponding rest-frame UV LFs are calculated as:

$$\phi(M_{\rm UV}) = \left[f_{\rm duty}\frac{{\rm d}n}{{\rm d}M_{\rm h}}\right]\left|\frac{{\rm d}M_{\rm h}}{{\rm d}M_{\rm UV}}\right|, \quad (6)$$

where ${\rm d}n/{\rm d}M_{\rm h}$ is the halo mass function. To calculate the ${\rm d}M_{\rm h}/{\rm d}M_{\rm UV}$ term, we assume a linear dependence of the 1500 Å UV luminosity to the SFR: $\dot{M}_*(M_{\rm h}, z) = \mathcal{K}_{\rm UV} \times L_{\rm UV}$, just as we did when constructing the mock LFs from the GAFFER simulations.

We thus have six free parameters which regulate the emission of UV photons: $f_{*,\,10}$, α_*, $f_{\rm esc,\,10}$, $\alpha_{\rm esc}$, $M_{\rm turn}$, and t_*. We introduce two additional parameters to characterize the X-ray emission of high-z galaxies, $L_{\rm X<2\,keV}/{\rm SFR}$ and E_0, which we describe below.

It is expected that X-rays, through their long mean-free paths, are a dominant source of heat in the neutral IGM, outside of the H II regions which surround the nascent galaxies (e.g. Pritchard & Furlanetto 2007; McQuinn & O'Leary 2012; Mesinger, Ferrara & Spiegel 2013; Madau & Fragos 2017; Eide et al. 2018). 21CMFAST computes the angle-averaged specific X-ray intensity (in units of erg s^{-1} keV^{-1} cm^{-2} sr^{-1}) in each simulation cell at a given spatial position and redshift. We parametrize the typical emerging X-ray spectral energy distribution of high- z galaxies via their integrated soft-band (< 2keV) luminosity per SFR (in units of erg s^{-1} M$_\odot^{-1}$ yr),

$$L_{\rm X<2\,keV}/{\rm SFR} = \int_{E_0}^{2\,{\rm keV}} {\rm d}E_{\rm e}\, L_{\rm X}/{\rm SFR}, \quad (7)$$

where $L_{\rm X}/{\rm SFR}$ is the specific X-ray luminosity per unit star formation escaping the host galaxies in units of erg s^{-1} keV^{-1} M$_\odot^{-1}$ yr, taken here to be a power law with energy index $\alpha_{\rm X} = 1$ (e.g. Fragos et al. 2013; Mineo, Gilfanov & Sunyaev 2012; Das et al. 2017) and E_0 is an additional free parameter corresponding to the X-ray energy threshold below which photons are absorbed inside the host galaxies, never managing to escape and heat the IGM.

We compute a mock observation from a simulation box of 500 Mpc on a side with a 256^3 grid, downsampled from 1024^3 initial conditions. Our default astrophysical parameters used for the mock simulation are listed in Table 1; these parameters are consistent with the mock UV LFs as shown below and discussed in Gillet at al. (in preparation).

From the light-cone of this simulation, we compute the 3D PS in 12 segments, sliced along the redshift/frequency axis in equal comoving volumes. As in Park et al. (2019), we compute the thermal and cosmic variance noise on the PS at each redshift using the public code 21CMSENSE[5] (Pober et al. 2013, 2014). For this, we assume the 'moderate' foreground removal strategy from Pober et al. (2014) which restricts the computation of the 21cm PS to modes outside of the foreground 'wedge'. Further, this assumes coherent summation over redundant baselines in order to reduce thermal noise (Parsons et al. 2012). For this work, we assume a single 1000 h tracked scan with the SKA. We model the SKA using the recent SKA System Baseline Design document.[6]

3 RESULTS

We combine the above-mentioned data sets within a fully Bayesian framework, obtaining parameter constraints with the public Monte Carlo Markov Chain (MCMC) sampler of 3D EoR/CD simulations, 21CMMC[7] (Greig & Mesinger 2015, 2017b; Greig & Mesinger 2018). At each parameter sample, 21CMMC computes the corresponding 21-cm PS, UV LFs, and reionizaton history, comparing them with our data sets using a χ^2 likelihood and a flat prior over the

[5]https://github.com/jpober/21cmSense
[6]http://astronomers.skatelescope.org/wp-content/uploads/2016/09/SKA-TEL-SKO-0000422_02_SKA1_LowConfigurationCoordinates-1.pdf
[7]https://github.com/BradGreig/21CMMC

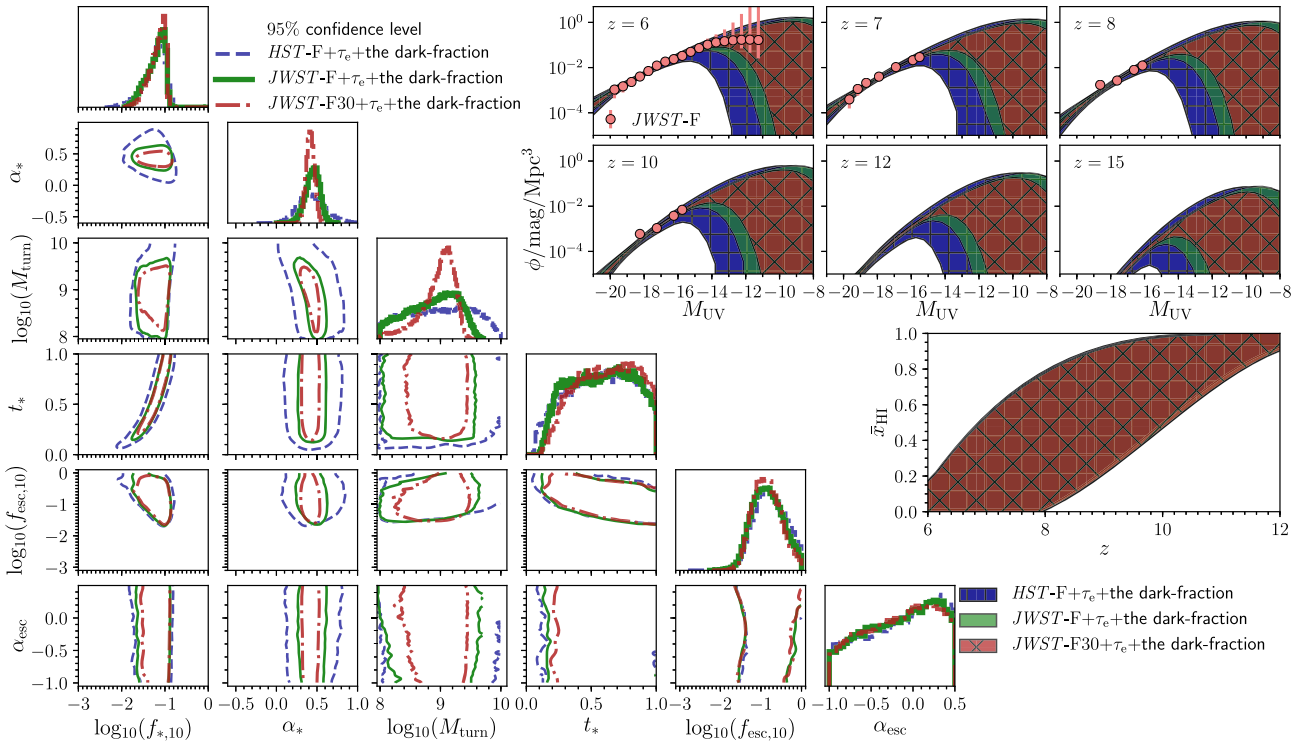

Figure 3. Corner plot showing parameter constrains for the mock UV LFs (see legend): 1D marginalized PDFs and 2D marginalized joint posterior distributions are shown along the diagonal and in the bottom left corner, respectively. Blue dashed, green solid, and brown dotted–dashed lines represent 95 per cent confidence levels for constraints using data sets of the mock *HST*-F, the mock *JWST*-F, and the mock *JWST*-F30, respectively. Top right panels: recovered 95 per cent confidence levels of the LFs corresponding to the posterior of our model. Shaded regions with the cross hatch (blue, '+'), shaded regions (green), and shaded regions with '×' hatch (brown) represent constraints using the mock *HST*-F, the mock *JWST*-F, and the mock *JWST*-F30, respectively. Middle right: corresponding constraints on the global evolution of the IGM neutral fraction, $x_{\rm HI}(z)$ with the same legends (note that these almost entirely overlap, highlighting that improved LF constraints will not aid in nailing down the EoR history, provided the escape fraction is allowed to be a free functional). Note that together with the listed data sets we also use (i) the electron scattering optical depth to the CMB from Planck Collaboration et al. (2016b); and (ii) the upper limit of the neutral fraction at $z = 5.9$ from the dark fraction of pixels in QSO spectra (McGreer et al. 2015).

parameter ranges shown in the figures below. The likelihoods for each data set are multiplied together when computing the posterior. For the 21-cm PS, we include a 20 per cent Gaussian error on the PS in each bin to account for simulation inaccuracy (e.g. Zahn et al. 2011), adding it in quadrature with the sample variance. For all runs, we include the additional EoR timing constraints mentioned above: (i) the electron scattering optical depth to the CMB $\tau_{\rm e} = 0.058 \pm 0.012 (1\sigma)$ from Planck Collaboration et al. (2016b); and (ii) the upper limit of the neutral fraction $\bar{x}_{\rm HI} < 0.06 + 0.05\,(1\sigma)$ at $z = 5.9$ from McGreer et al. (2015).

3.1 Constraints using LFs without 21 cm

3.1.1 Assuming an intrisic turnover at fainter magnitudes

In Fig. 3, we show constraints on our six astrophysical parameters describing the UV emission of galaxies: $f_{*,\,10}$, α_*, $f_{\rm esc,\,10}$, $\alpha_{\rm esc}$, $M_{\rm turn}$, and t_*, constructed using the 'faint end' turnover LFs, for both *HST* and *JWST*. As discussed previously, if the turnover is at faint magnitudes, it is more difficult to be detectable even with *JWST*; therefore the '-F' LFs can be considered the 'pessimistic' scenario.

The marginalized posteriors are shown in the corner plot on the left-hand side, while the corresponding recovered UV LFs are shown in the upper right, with the EoR history in the middle right. As noted in the legend, blue/green lines and shaded areas denote posteriors constructed using *HST*-F/*JWST*-F data sets. All data sets additionally include $\tau_{\rm e}$ and the dark fraction measurements. The marginalized 1D constraints are also written in Table 2.

Using *HST*-F LFs, we recover the trends already noted in Park et al. (2019). Although here we use a mock *HST*-F observation to directly compare against the *JWST*-F forecast, the mock *HST*-F is by construction consistent with current observations (cf. Fig. 1), and so the agreement with Park et al. (2019) is understandable. Most notably, we find that *HST*-F LFs are unable to constrain the flattening/turnover scale, $M_{\rm turn}$, encoding the halo mass below which star formation becomes inefficient. They only provide an upper limit, ruling out $\log_{10}(M_{\rm turn}) \lesssim 9.88$ at 95 per cent confidence level. The constraints on the scaling of the stellar mass with halo mass is reasonable, with a fractional uncertainty in the relevant parameters of order tens of per cent (cf. Table 1).[8] The ionizing

[8] A careful reader can note that the recovered fractional uncertainty on α_* is a factor of two larger than quoted in Park et al. (2019). This is due to the fact that our mock observation comes from a fairly small simulation box, 10 Mpc on a side. The resulting Poisson noise for the brightest galaxies is larger than was quoted in the Bouwens et al. (2016) observations that were used in Park et al. (2019), resulting in weaker recovery on the halo mass scaling of the stellar mass.

Table 2. Summary of the median recovered values with $1\,\sigma$ errors for the eight free parameters, obtained from our MCMC procedure for each combination of data sets listed below. Note that together with the listed data sets we also use (i) the electron scattering optical depth to the CMB from Planck Collaboration et al. (2016b); and (ii) the upper limit of the neutral fraction at $z = 5.9$ from the dark fraction of pixels in QSO spectra (McGreer et al. 2015). We note that the fiducial values are used for generating the mock 21-cm signal; LFs are taken independently from the GAFFER simulations.

	Parameters							
	$\log_{10}(f_{*,\,10})$	α_*	$\log_{10}(f_{\rm esc,\,10})$	$\alpha_{\rm esc}$	$\log_{10}(M_{\rm turn})$ ($\rm M_\odot$)	t_*	$\log_{10}\left(\frac{L_{\rm X<2keV}}{\rm SFR}\right)$ ($\rm erg\,s^{-1}\,M_\odot^{-1}\,yr$)	E_0 (keV)
Fiducial values (21-cm only)	-1.155	0.38	-1.155	-0.20	9.00	0.6	40.50	0.50
HST-F	$-1.19^{+0.18}_{-0.31}$	$0.44^{+0.18}_{-0.15}$	$-0.79^{+0.43}_{-0.38}$	$-0.09^{+0.42}_{-0.57}$	$9.02^{+0.56}_{-0.63}$	$0.58^{+0.26}_{-0.29}$	–	–
JWST-F	$-1.17^{+0.16}_{-0.28}$	$0.45^{+0.08}_{-0.09}$	$-0.85^{+0.41}_{-0.37}$	$-0.11^{+0.42}_{-0.54}$	$8.92^{+0.38}_{-0.52}$	$0.59^{+0.26}_{-0.28}$	–	–
JWST-F30	$-1.15^{+0.14}_{-0.23}$	$0.42^{+0.05}_{-0.05}$	$-0.87^{+0.37}_{-0.33}$	$-0.12^{+0.41}_{-0.53}$	$9.02^{+0.19}_{-0.33}$	$0.63^{+0.24}_{-0.26}$	–	–
HST-B	$-1.29^{+0.19}_{-0.29}$	$0.36^{+0.14}_{-0.12}$	$-0.64^{+0.38}_{-0.39}$	$-0.14^{+0.44}_{-0.55}$	$9.11^{+0.53}_{-0.65}$	$0.59^{+0.26}_{-0.27}$	–	–
JWST-B	$-1.24^{+0.16}_{-0.26}$	$0.38^{+0.09}_{-0.09}$	$-0.62^{+0.33}_{-0.33}$	$-0.15^{+0.45}_{-0.53}$	$9.40^{+0.18}_{-0.36}$	$0.61^{+0.25}_{-0.27}$	–	–
21-cm + *JWST*-F	$-1.19^{+0.12}_{-0.15}$	$0.44^{+0.07}_{-0.06}$	$-1.16^{+0.16}_{-0.13}$	$-0.21^{+0.10}_{-0.10}$	$8.92^{+0.11}_{-0.10}$	$0.57^{+0.17}_{-0.16}$	$40.49^{+0.04}_{-0.04}$	$0.50^{+0.02}_{-0.02}$

escape fraction is only poorly constrained, with the normalization parameter $f_{\rm esc,\,10}$ having a 1σ fractional uncertainty of $\sim$50 per cent, while its dependence on halo mass is completely unconstrained (as evidenced by the flat marginalized probability density function (PDF) over $\alpha_{\rm esc}$, consistent with our priors).

Considering the *JWST*-F LFs, we note that the constraints are not very different for the escape function parameters (as is expected since we are not directly adding information on the ionizing photon budget). However, the recovery of parameters describing star formation is (modestly) improved. Specifically, we note that the 1σ fractional uncertainty for α_* is reduced by a factor of 2. This is because the reduced errors of the mock *JWST* LFs tighten the slope of the LFs (see Fig. 2). Together with the reduced errors, the extended faint end provides additional information on the abundance of faint galaxies, which translates to a somewhat tighter upper limit on $\log_{10}(M_{\rm turn}) \lesssim 9.53$ at 95 per cent confidence level. This improvement is more notable when looking at the corresponding recovered LFs in the upper right panels. We see explicitly that our mock *JWST*-F LFs allow us to rule out models which predict a turnover at $M_{\rm UV} < -13$.

3.1.2 *Would reduced observational uncertainties improve constraints?*

In the previous section, we noted that *if* the intrinsic LFs turn over at faint magnitudes ($M_{\rm UV} \gtrsim -12$), *JWST* LFs will only modestly improve on our current knowledge of average galaxy properties, as obtained with *HST* LFs. The largest improvement comes in the form of improved constraints on α_* and a somewhat tighter upper limit on the turnover scale.

Here, we consider a more 'optimistic' *JWST*-F forecast, labeled *JWST*-F30. This forecast is based on the same intrinsic LFs, '-F', but we assume that uncertainties can be reduced, e.g. due to an improved understanding of the dominant systematic uncertainties. To illustrate this, we simply reduce the errors of each LF bin to 30 per cent of their fiducial values, discussed previously, keeping the 20 per cent minimum error. In other words, in each magnitude bin we take $\sigma_{JWST-F30} = \max[\sigma_{JWST-F}, 0.2\phi]$.

Fig. 4 shows the resulting *JWST* LFs, and the corresponding parameter constraints are shown in Fig. 3 with the label *JWST*-F30. The most notable improvement is on $\log_{10}(M_{\rm turn})$. As evidenced by the 1D PDF, the constraints on the turnover mass are significantly

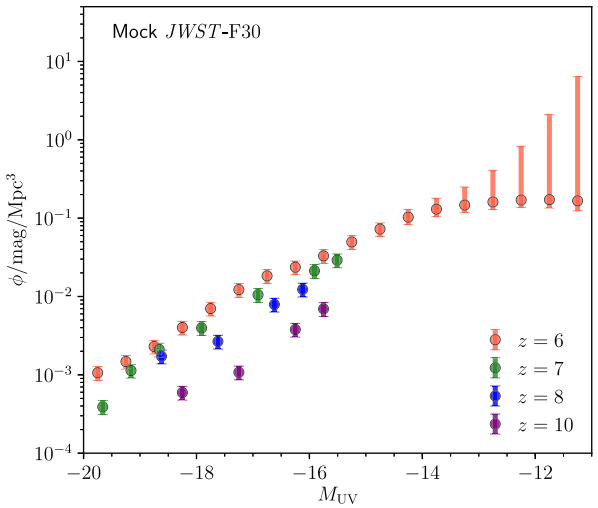

Figure 4. Mock LFs assuming an optimistic error budget, obtained by reducing the fiducial *JWST* uncertainties by 30 per cent. The intrinsic number densities are taken from the faint turnover model.

tightened, which is in contrast to the mock *JWST*-F LFs which only provide an upper limit. Moreover, the 1σ fractional uncertainty for α_* is reduced by $\sim$60 per cent, compared with the mock *JWST*-F LFs.

3.1.3 *Assuming an intrinsic turnover at brighter magnitudes*

We now show the resulting constraints for the mock LFs with the turnover at brighter magnitudes (i.e. *HST*-B and *JWST*-B from Fig. 2) in Fig. 5. Comparing *JWST*-B results to those of *JWST*-F, we note a large improvement in the inference of the turnover scale. This is understandable, since the '-B' LFs intrinsically turn over at scales which approach the *JWST* sensitivity thresholds. This is reflected also in the recovered LFs (upper right panels in Fig. 5), which understandably show stronger evidence of a turnover than was the case for *JWST*-F in the previous figure. Specifically, we recover $\log_{10}(M_{\rm turn}) = 9.40^{+0.18}_{-0.36}$ (1σ). This fractional uncertainty of $\sim$3 per cent is comparable to the constrains achievable with the reduced error bar LFs discussed in Section 3.1.2. Therefore, signif-

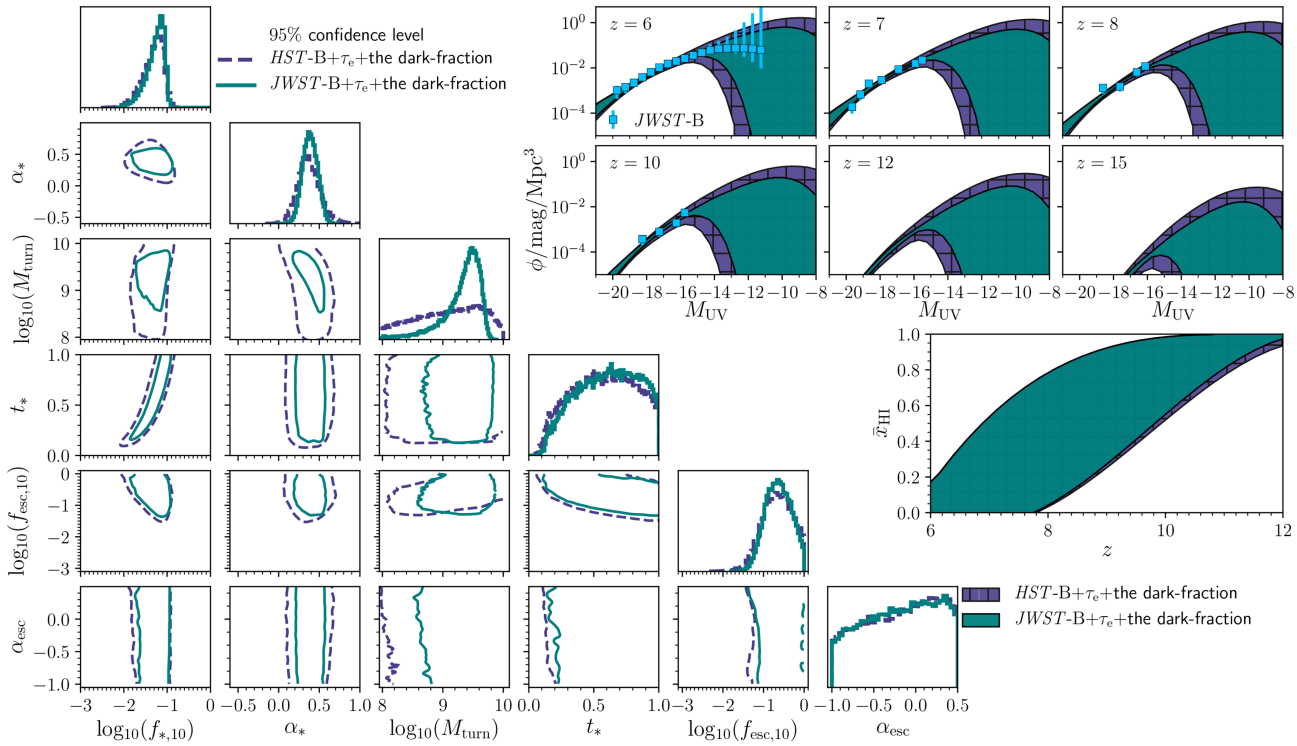

Figure 5. The same as Fig. 3, but for the mock *HST*-B and *JWST*-B LFs. Purple dashed and turquoise solid lines represent 95 per cent confidence levels for constraints using data sets of the mock *HST*-B and the mock *JWST*-B, respectively. Shaded regions with the cross hatch (purple, '+') and shaded regions (turquoise) represent constraints using the mock *HST*-B and the mock *JWST*-F, respectively.

icant improvement in the inference of faint-end galaxy properties is likely with *JWST* if *either* we are able to better characterize systematic lensing uncertainties than currently possible, *or* the intrinsic LFs peak at $M_{\rm UV} \lesssim -13$.

3.2 Combined constraints with LFs and 21-cm signals

In the previous sections, we saw that if the LFs turn over at $M_{\rm UV} \gtrsim -12$ (our '-F' models), a dramatic improvement in inference using *JWST* observations is unlikely, given our fiducial uncertainties. Here, we additionally add mock 21-cm PS observations, to see if parameter inference is improved, for these 'pessimistic' LFs. We also extend our parameter space to include the aforementioned X-ray parameters, which drive the Epoch of Heating, observable with 21 cm.

The resulting corner plot is shown in Fig. 6. Adding the mock 21-cm observation results in a marked improvement in all parameter constraints, as expected from Park et al. (2019). We find the 21-cm signal dominates constraints on $\log_{10}(M_{\rm turn})$, t_*, $\log_{10}(f_{\rm esc,\,10})$, $\alpha_{\rm esc}$, $\log_{10}(L_{\rm X<2\,keV}/{\rm SFR})$, and E_0. On the other hand, the LFs dominates constraints on α_*, as evidenced by the almost identical 1D PDFs of α_* from the mock 21-cm + *JWST*-F LFs and from the mock *JWST*-F LFs only. Constraints on $f_{*,\,10}$ are comparably sourced by both observations. In summary, the $1\,\sigma$ fractional uncertainties on our parameters from the combined data sets are $[\log_{10}(f_{*,\,10})$, α_*, $\log_{10}(f_{\rm esc,\,10})$, $\alpha_{\rm esc}$, $\log_{10}(M_{\rm turn})$, t_*, $\log_{10}(L_{\rm X<2\,keV}/{\rm SFR})$, $E_0] = (11,\ 15,\ 13,\ 47,\ 1.0,\ 29,\ 0.1,\ 4.6)$ per cent.

The most dramatic improvement is seen in the EoR history (middle right panel). With 21-cm observations, we will know the EoR history to within $\Delta z(\bar{x}_{\rm HI}) \lesssim 0.1$ (1σ) over most of the EoR. This is a order of magnitude improvement over our current state of knowledge: $\Delta z(\bar{x}_{\rm HI}) \lesssim 1$.

4 CONCLUSIONS

Next generation observatories will enable us to study the first billion years of our Universe in unprecedented detail. Foremost among these are 21-cm interferometry with HERA and SKA, and high-z galaxy observations with *JWST*. Here, we quantify how observations from these instruments can be used to constrain the astrophysics of high-z galaxies. For this purpose, we generate mock *JWST* LFs, based on two different hydrodynamical cosmological simulations; these have intrinsic LF which turn over at different scales and yet are fully consistent with present-day observations. Likewise, we generate mock 21-cm PS, using the seminumerical code 21CMFAST combined with a moderate foreground model and 1000 h thermal noise with the SKA1-low instrument. We assume a simple astrophysical model for the high-z galaxy population, in which the SFR and ionizing escape fraction are power-law functions of halo mass, and there is an exponential suppression of star-forming galaxies below some threshold halo mass.

We find that if the LFs turn over at magnitudes fainter than $M_{\rm UV} \gtrsim -12$, we must significantly improve on our understanding of systematic lensing uncertainties in order for *JWST* LFs to dramatically improve our understanding of the faint galaxies, beyond what we have currently with *HST* LFs. However, if LFs intrinsically turn over at magnitudes brighter than $M_{\rm UV} \lesssim -13$, then the turn over scale can be easily recovered to within a few per cent, and uncertainties on the SFR to halo mass relation can be decreased by ~ 50 per cent.

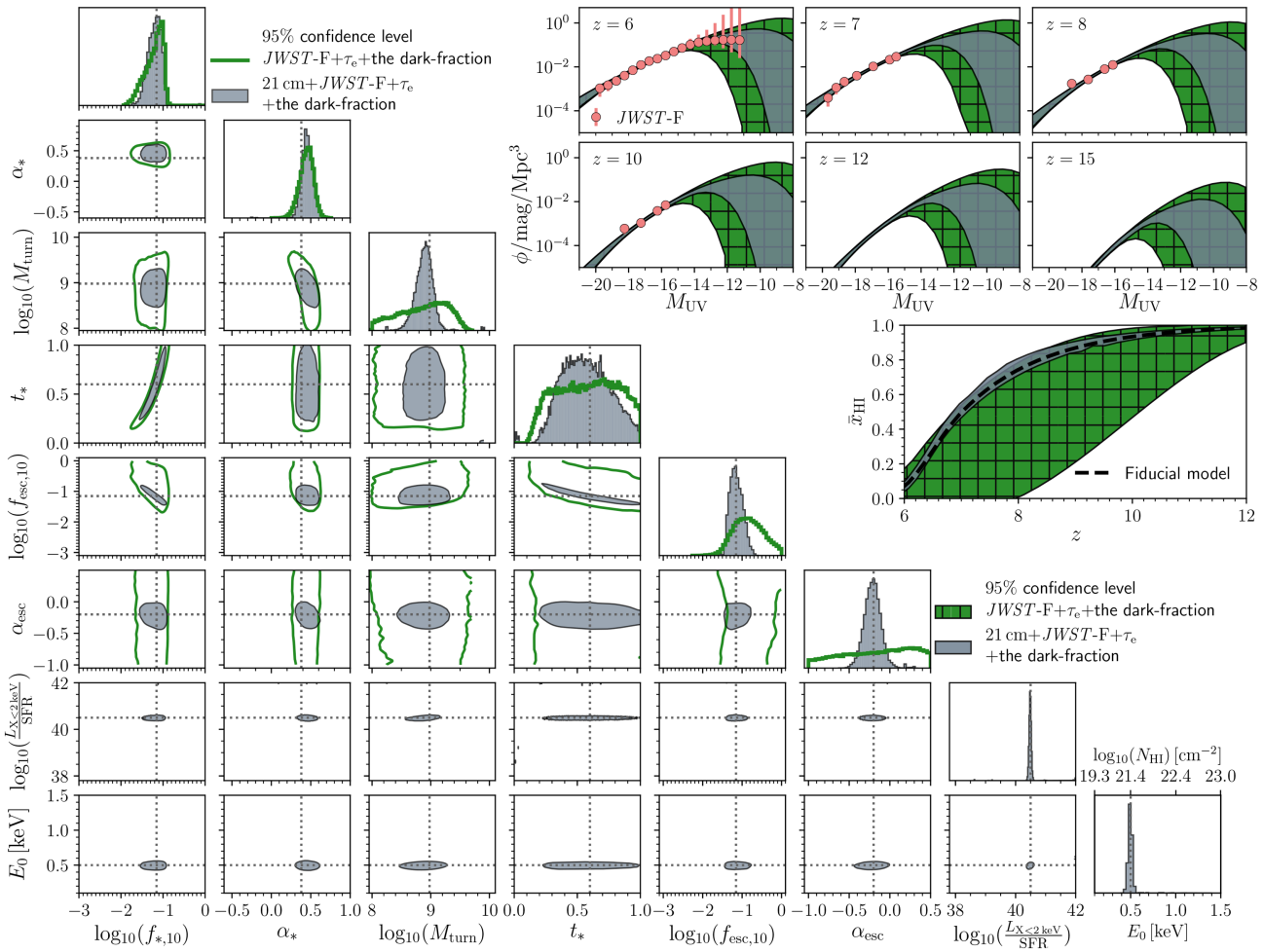

Figure 6. Same as Fig. 3, but including also constraints available from adding mock 21-cm observations (see the legend).

Additionally including 21-cm observations would improve constraints significantly, even for our most pessimistic *JWST* scenario. The two observations are complementary, with *JWST* dominating constraints on the SFR-to-halo mass relation, and 21-cm dominating constraints on the ionizing escape fraction, turn over scale, and the EoR history.

ACKNOWLEDGEMENTS

We thank R. Bouwens, S. Finkelstein, and P. Oesch for enlightening discussions about approximating *JWST* LF uncertainties. This project has received funding from the European Research Council (ERC) under the European Union's Horizon 2020 research and innovation program (grant agreement no. 638809 – AIDA – PI: Mesinger). The results presented here reflect the authors' views; the ERC is not responsible for their use. The simulations used to generate the mock LFs were computed as part of the PRACE tier-0 grant GAFFER (project no. 2016163945). We acknowledge PRACE for awarding us access to Curie at GENCI@CEA, France.

REFERENCES

Atek H. et al., 2015, ApJ, 800, 18
Atek H., Richard J., Kneib J.-P., Schaerer D., 2018, MNRAS, 479, 5184
Aubert D., Deparis N., Ocvirk P., 2015, MNRAS, 454, 1012
Bañados E. et al., 2018, Nature, 553, 473
Barkana R., Loeb A., 2001, Phys. Rep., 349, 125
Behroozi P. S., Silk J., 2015, ApJ, 799, 32
Bouwens R. J. et al., 2015a, ApJ, 803, 1
Bouwens R. J., Illingworth G. D., Oesch P. A., Caruana J., Holwerda B., Smit R., Wilkins S., 2015b, ApJ, 811, 140
Bouwens R. J., Oesch P. A., Illingworth G. D., Ellis R. S., Stefanon M., 2016, ApJ, 843, 129
Chevallard J. et al., 2019, MNRAS, 483, 2621
Cowley W. I., Baugh C. M., Cole S., Frenk C. S., Lacey C. G., 2018, MNRAS, 474, 2352
Cullen F., McLure R. J., Khochfar S., Dunlop J. S., Dalla Vecchia C., 2017, MNRAS, 470, 3006
Das A., Mesinger A., Pallottini A., Ferrara A., Wise J. H., 2017, MNRAS, 469, 1166
Dayal P., Ferrara A., 2018, Phys. Rep., 780, 1
Dayal P., Dunlop J. S., Maio U., Ciardi B., 2013, MNRAS, 434, 1486
DeBoer D. R. et al., 2017, PASP, 129, 045001
Deparis N., Aubert D., Ocvirk P., 2016, in Reylè C., Richard J., Cambrèsy L., Deleuil M., Pècontal E., Tresse L., Vauglin I., eds, SF2A-2016: Proceedings of the Annual Meeting of the French Society of Astronomy and Astrophysics, p. 399
Deparis N., Aubert D., Ocvirk P., Chardin J., Lewis J., 2019, A&A, 622, A142
Dunlop J. S. et al., 2013, MNRAS, 432, 3520
Eide M. B., Graziani L., Ciardi B., Feng Y., Kakiichi K., Di Matteo T., 2018, MNRAS, 476, 1174

Finkelstein S. L. et al., 2012, ApJ, 756, 164
Finkelstein S. L., 2016, PASA, 33, e037
Fragos T. et al., 2013, ApJ, 764, 41
Furlanetto S. R., Zaldarriaga M., Hernquist L., 2004, ApJ, 613, 1
Gardner J. P. et al., 2006, Space Sci. Rev., 123, 485
Gillet N. J. F., Mesinger A., Park J., 2019, MNRAS, 491, 1980
Giroux M. L., Sutherland R. S., Shull J. M., 1994, ApJ, 435, L97
Gorce A., Douspis M., Aghanim N., Langer M., 2018, A&A, 616, A113
Greig B., Mesinger A., 2015, MNRAS, 449, 4246
Greig B., Mesinger A., 2017a, MNRAS, 465, 4838
Greig B., Mesinger A., 2017b, MNRAS, 472, 2651
Greig B., Mesinger A., 2018, MNRAS, 477, 3217
Hui L., Gnedin N. Y., 1997, MNRAS, 292, 27
Ishigaki M., Kawamata R., Ouchi M., Oguri M., Shimasaku K., Ono Y., 2018, ApJ, 854, 73
Keating L. C., Weinberger L. H., Kulkarni G., Haehnelt M. G., Chardin J., Aubert D., 2019, preprint (arXiv:1905.12640)
Kennicutt R. C., Jr., 1998, ARA&A, 36, 189
Koopmans L. et al., 2015, Proceedings of Science, Vol. 215, Advancing Astrophyscis with the Square Kilometre Array (AASKA14), p. 1
Kuhlen M., Faucher-Giguère C. A., 2012, MNRAS, 423, 862
Lidz A., McQuinn M., Zaldarriaga M., Hernquist L., Dutta S., 2007, ApJ, 670, 39
Livermore R. C., Finkelstein S. L., Lotz J. M., 2017, ApJ, 835, 113
Ma X. et al., 2019, MNRAS, 487, 1844
Madau P., Dickinson M., 2014, ARA&A, 52, 415
Madau P., Fragos T., 2017, ApJ, 840, 39
McGreer I. D., Mesinger A., D'Odorico V., 2015, MNRAS, 447, 499
McQuinn M., O'Leary R. M., 2012, ApJ, 760, 3
McQuinn M., Lidz A., Zahn O., Dutta S., Hernquist L., Zaldarriaga M., 2007, MNRAS, 377, 1043
Mellema G. et al., 2013, Exp. Astron., 36, 235
Mesinger A., 2010, MNRAS, 407, 1328
Mesinger A., Dijkstra M., 2008, MNRAS, 390, 1071
Mesinger A., Furlanetto S., 2007, ApJ, 669, 663
Mesinger A., Furlanetto S., Cen R., 2011, MNRAS, 411, 955
Mesinger A., Ferrara A., Spiegel D. S., 2013, MNRAS, 431, 621
Mineo S., Gilfanov M., Sunyaev R., 2012, MNRAS, 419, 2095
Mitra S., Ferrara A., Choudhury T. R., 2013, MNRAS, 428, L1
Mitra S., Roy Choudhury T., Ferrara A., 2015, MNRAS, 454, L76
Mortlock D. J. et al., 2011, Nature, 474, 616
O'Shea B. W., Wise J. H., Xu H., Norman M. L., 2015, ApJ, 807, L12
Oesch P. A., Bouwens R. J., Illingworth G. D., Labbe I., Stefanon M., 2017, ApJ, 855, 105
Okamoto T., Gao L., Theuns T., 2008, MNRAS, 390, 920
Park J., Mesinger A., Greig B., Gillet N., 2019, MNRAS, 484, 933
Parsons A., Pober J., McQuinn M., Jacobs D., Aguirre J., 2012, ApJ, 753, 81
Planck Collaboration XIII et al., 2016a, A&A, 594, A13
Planck Collaboration XLVII et al., 2016b, A&A, 596, A108
Planck Collaboration VI et al., 2018, preprint (arXiv:1807.06209)
Pober J. C. et al., 2013, AJ, 145, 65
Pober J. C. et al., 2014, ApJ, 782, 66
Pober J. C. et al., 2015, ApJ, 809, 62
Price D. C. et al., 2018, MNRAS, 478, 4193
Price L. C., Trac H., Cen R., 2016, preprint (arXiv:1605.03970)
Pritchard J. R., Furlanetto S. R., 2007, MNRAS, 376, 1680
Robertson B. E. et al., 2013, ApJ, 768, 71
Robertson B. E., Ellis R. S., Furlanetto S. R., Dunlop J. S., 2015, ApJ, 802, L19
Ross H. E., Dixon K. L., Ghara R., Iliev I. T., Mellema G., 2019, MNRAS, 491, 1101
Salcido J., Bower R. G., Theuns T., 2019, preprint (arXiv:1908.00552)
Salvaterra R., Ferrara A., Dayal P., 2011, MNRAS, 414, 847
Scoccimarro R., 1998, MNRAS, 299, 1097
Shapiro P. R., Giroux M. L., Babul A., 1994, ApJ, 427, 25
Shapley A. E. et al., 2017, ApJ, 846, L30
Shimizu I., Inoue A. K., Okamoto T., Yoshida N., 2014, MNRAS, 440, 731
Sobacchi E., Mesinger A., 2013, MNRAS, 432, L51
Springel V., Hernquist L., 2003, MNRAS, 339, 312
Stark D. P., 2016, ARA&A, 54, 761
Sun G., Furlanetto S. R., 2016, MNRAS, 460, 417
Tacchella S., Bose S., Conroy C., Eisenstein D. J., Johnson B. D., 2018, ApJ, 868, 92
Vogelsberger M. et al., 2019, preprint (arXiv:1904.07238)
Wilkins S. M., Feng Y., Di Matteo T., Croft R., Lovell C. C., Waters D., 2017, MNRAS, 469, 2517
Williams C. C. et al., 2018, ApJS, 236, 33
Yung L. Y. A., Somerville R. S., Finkelstein S. L., Popping G., Davé R., 2019, MNRAS, 483, 2983
Zahn O., Mesinger A., McQuinn M., Trac H., Cen R., Hernquist L. E., 2011, MNRAS, 414, 727

SUPPORTING INFORMATION

Supplementary data are available at *MNRAS* online.

parameter_variation.mp4

Please note: Oxford University Press is not responsible for the content or functionality of any supporting materials supplied by the authors. Any queries (other than missing material) should be directed to the corresponding author for the article.

This paper has been typeset from a TEX/LATEX file prepared by the author.